processes

MDPI

Article

Surrogate-Based Constrained Single-Objective Bayesian Optimization for Joule-Heated Methane Dry Reforming Reactors

Yanlun Ren [1,*], Daqing Tang [2], Li Zhang [2], Houfang Miao [1], Meiying Cui [1], Zhiwei Li [1] and Xuqiang Ding [1]

[1] School of Automotive Engineering, Nantong Institute of Technology, Nangtong 226000, China
[2] School of Mechanical and Power Engineering, East China University of Science and Technology, Shanghai 200237, China
* Correspondence: renyanlun@163.com

Abstract

Joule heating coupled with porous media offers rapid in situ heat generation and a more uniform temperature distribution for DRM reactions, whereas the strong coupling of structural and operating parameters renders conventional trial-and-error optimization inefficient and costly. To tackle this challenge, a multi-physics numerical model for a centrally resistively heated DRM reactor is constructed by coupling Joule heating, flow and heat transfer, multi-component species transport, and apparent reaction kinetics. A fully connected feedforward neural network (FC-FNN) surrogate model is further established to enable rapid prediction of reactor performance. Seven critical input variables are selected, including reaction temperature, gas hourly space velocity (GHSV), etc., and 9216 simulation samples are generated via numerical simulations for surrogate model training and parametric analysis. The results demonstrate that the Bayesian-optimized FC-FNN model exhibits high predictive accuracy for the core reactor performance metrics, achieving coefficients of determination (R^2) above 0.960 for CH_4 conversion, CO_2 conversion, energy efficiency, and the H_2/CO molar ratio. Subsequently, an unknown-constrained alternating Bayesian optimization (UCA-BO) algorithm is adopted to maximize the average reactant conversion under the constraints of H_2/CO molar ratio ≥ 0.9 and bed-temperature non-uniformity $\leq 5\%$. Under the optimized operating conditions, the average reactant conversion reaches 94.12%, accompanied by a H_2/CO molar ratio of 0.98, a bed-temperature non-uniformity of 4.53%, and a system energy efficiency of 74.83%. Posterior verification with the trained surrogate model gives slightly lower values (91.28%, 0.91, 4.86%, and 72.36%), all of which remain within the imposed constraints, confirming feasibility. Overall, the proposed integrated framework of numerical simulation, surrogate modeling, and Bayesian optimization enables efficient parameter screening and comprehensive performance optimization of resistively heated porous-media DRM systems, providing a methodological basis for the structural design and operating-parameter optimization of related reactor systems.

Keywords: dry reforming of methane; Joule heating; porous medium; neural network; Bayesian optimization

Check for updates

Academic Editor: Iqbal M. Mujtaba

Received: 23 August 2026
Revised: 26 September 2026
Accepted: 14 October 2026
Published: 3 November 2026

Copyright: © 2026 by the authors. Licensee MDPI, Basel, Switzerland. This article is an open access article distributed under the terms and conditions of the Creative Commons Attribution (CC BY) license.

1. Introduction

Dry reforming of methane (DRM, $CH_4 + CO_2 \rightarrow 2H_2 + 2CO$) enables simultaneous conversion of the two greenhouse gases, CH_4 and CO_2, while producing syngas with a theoretical H_2/CO molar ratio close to unity. Accordingly, it has attracted considerable attention for low-carbon hydrogen production and carbon resource recycling [1–3]. Nevertheless, the DRM reaction is strongly endothermic and requires high temperatures to

achieve high reactant conversion. Additionally, side-reactions including reverse water–gas shift, methane cracking, and CO disproportionation may occur during operation, altering the syngas composition and triggering catalyst coking [4–6].

Conventional fixed-bed DRM reactors rely predominantly on external heating, in which heat is transferred from the reactor wall toward the interior of the catalyst bed, readily resulting in radial and axial temperature gradients. Localized low-temperature regions can limit reactant conversion, whereas excessive local temperatures may accelerate catalyst sintering and carbon deposition. Therefore, process intensification of DRM requires not only regulation of catalyst activity but also comprehensive optimization of the heating strategy, bed structure, and operating conditions.

Electrified heating offers a new strategy for intensifying high-temperature endothermic reactions. Compared with conventional external heating, Joule heating converts electric energy into heat within the reaction zone directly, shortening heat-transfer pathways and accelerating the thermal response [7–9]. Porous media feature interconnected three-dimensional pores, large specific surface area, and favorable gas–solid contact, which enhance heat and mass transfer and flow distribution inside the bed [10–13]. Accordingly, integrating Joule heating with porous-medium structures holds great potential to mitigate insufficient heat supply and uneven temperature distribution in DRM systems.

The resistively heated porous-medium DRM system involves multi-variable coupling among reaction temperature, gas hourly space velocity, feed ratio, operating pressure, porosity, pore size and input power. Large-scale numerical simulations and experimental optimization incur high costs. Artificial neural networks can learn rapid nonlinear mappings between input parameters and reaction performance, while Bayesian optimization is competent for searching high-performance parameter spaces with limited evaluation runs. Both approaches have been applied to DRM performance prediction, catalyst screening, and reaction-condition optimization [14–16].

However, these approaches have largely been used in isolation; integrating them for constrained multi-parameter optimization of resistively heated porous-media DRM reactors, where operating and structural parameters are tightly coupled, remains unexplored. Here, we present an integrated workflow that combines multi-physics simulation with neural-network surrogate modeling, Bayesian optimization, and posterior verification to systematically probe the effects of operating conditions and porous-structure parameters on DRM performance and to maximize average reactant conversion under H_2/CO-ratio and temperature-uniformity constraints. This framework provides a transferable data-driven paradigm for electrified reactors and the design of renewable-powered, low-carbon DRM systems.

2. Numerical Model and Research Methodology

2.1. Numerical Model of Resistively Heated Porous-Medium DRM

The reactor investigated is a porous-media methane dry reforming reactor equipped with a centrally positioned electric heating rod. A two-dimensional axisymmetric model is developed, in which the heating rod acts as the internal heat source, and the porous-medium domain acts as the primary site for the reaction and heat and mass transport. The model simultaneously accounts for Joule heating, gas flow, heat transfer, species transport, and apparent reaction kinetics. The porous medium is treated using an equivalent continuum, whose effects on reactor performance are described by the porosity, average pore diameter, effective thermal conductivity, and flow resistance.

Reactor performance is evaluated in terms of CH_4 conversion, CO_2 conversion, H_2/CO ratio of products, energy efficiency, maximum temperature, average temperature, and temperature non-uniformity within the reaction zone. Specifically, the reactant conversion

and H_2/CO ratio are adopted to evaluate reaction performance and syngas quality. Energy efficiency quantifies the conversion from input electric power to endothermic reaction heat; temperature non-uniformity characterizes the thermal-field distribution within the reaction zone, and smaller values correspond to a more uniform temperature distribution. Specifically, only the primary DRM reaction and the reverse water–gas shift (RWGS) side reaction were incorporated into the kinetic model, whereas methane cracking and the Boudouard coking reaction were excluded. The energy efficiency (η_c) and temperature non-uniformity (U_T) are defined as follows:

$$\eta_c = p_{chem}/P_{in} \times 100\% \quad (1)$$

$$U_T = (T_{max} - T_{avg})/T_{avg} \times 100\% \quad (2)$$

where p_{chem} denotes the thermal power consumed by chemical reactions inside the porous-medium reaction zone, P_{in} is the input power of electric heating; and Tmax and Tavg represent the maximum and average temperatures within the reaction zone, respectively.

$$X_{CH_4} = \frac{F_{CH_4,in} - F_{CH_4,out}}{F_{CH_4,in}} \times 100\% \quad (3)$$

$$X_{CO_2} = \frac{F_{CO_2,in} - F_{CO_2,out}}{F_{CO_2,in}} \times 100\% \quad (4)$$

$$X_{avg} = \frac{X_{CH_4} + X_{CO_2}}{2} \quad (5)$$

The average reactant conversion X_{avg} is defined as the arithmetic mean of methane conversion X_{CH_4} and carbon dioxide conversion X_{CO_2}, which are calculated from the inlet–outlet molar flow rates. $F_{CH_4,in}$, $F_{CO_2,in}$ are inlet molar flow rates; $F_{CH_4,out}$, $F_{CO_2,out}$ denote outlet molar flow rates of corresponding species. The reaction-rate expressions were taken from reference [17,18].

$$\frac{\partial(\rho_g u_i h_g)}{\partial x_i} = \frac{\partial}{\partial x_i}\left[\lambda_{eff}\frac{\partial T}{\partial x_i} - \sum_{c=1}^{n} h_c J_{c,i} + (\tau_{ij})_{eff} u_i\right] + S_r + S_s + S_c \quad (6)$$

$$\frac{\partial(\rho_g u_i c_{p,g} T)}{\partial x_i} = \frac{\partial}{\partial x_i}\left[(\lambda_g + \frac{c_{p,g}\mu_t}{Pr_t})\frac{\partial T}{\partial x_i} + (\tau_{ij})_{eff} u_i\right] + S_r \quad (7)$$

Sensible-heat transport was accounted for in the gas-phase energy equations, with the endothermic reaction heat and gas sensible heat given by Equations (6) and (7); convective and radiative heat-loss boundary conditions were imposed on the outer surface.

The governing equation of energy conservation is given by Equation (6), where S_s denotes the heat-source term absorbed in the porous-medium domain, S_c is the heat source associated with chemical reactions, h_c represents the specific enthalpy of species c, and λ_{eff} is the effective thermal conductivity of the electrically heated body, which can be determined from Equation (8). Within the pure gas-phase region, thermal energy transport is no longer governed by conduction alone but evolves into a composite mechanism in which conduction and forced convection are superimposed. The corresponding fluid energy conservation equation is given by Equation (7), where $c_{p,g}$ and λ_g denote the specific heat capacity at constant pressure and the thermal conductivity of the gas mixture, respectively, and S_r represents the radiative heat-source term.

$$\lambda_{eff} = \varphi(\lambda_g + \lambda_t) + (1 - \varphi)\lambda_s \quad (8)$$

where λg is the thermal conductivity of the gas mixture and λt is the turbulent thermal conductivity of the gas mixture. The P1 approximation radiation model given in Equation (9) is employed to calculate the radiative heat transfer within both the gas-phase region and

the porous absorber, and the corresponding radiative heat-source term (S_r) is determined from Equation (10).

$$\nabla(\frac{1}{3k}\nabla G) - k_a G + 4k_a n^2 \sigma T^4 = 0 \quad (9)$$

$$S_r = k_a G - 4k_a n^2 \sigma T^4 \quad (10)$$

where G is the incident radiation; n is the refractive index, set to a constant value of 1; and the extinction coefficient (κ), absorption coefficient (k_a), and scattering coefficient (k_s) for the different regions can be obtained from the corresponding equations [19], where ε is the emissivity of the porous absorber. The extinction, absorption, and scattering coefficients of the porous absorber are given by Equations (11)–(13).

$$k = k_a + k_s \quad (11)$$

$$k_a = \begin{cases} 1.5\varepsilon(1-\varphi)/d_p \\ 0 \end{cases} \quad (12)$$

$$k_s = \begin{cases} 1.5(2-\varepsilon)(1-\varphi)/d_p \\ 0 \end{cases} \quad (13)$$

The electric heating rod is made of Ni80Cr20 nickel–chromium alloy (80 wt% Ni and 20 wt% Cr). The thermal conductivity, specific heat capacity at constant pressure, and electrical conductivity of the heating rod are set to 20 W/(m·K), 480 J/(kg·K), and 9×10^5 S/m, respectively. The steady-state current conduction within the heating rod and the volumetric Joule heat source are shown in Equations (14)–(16).

$$\nabla \cdot J = 0 \quad (14)$$

$$J = -\sigma_e \nabla V \quad (15)$$

$$Q_j = J \cdot E = \sigma_e |\nabla V|^2 \quad (16)$$

where J is the current density, V is the electric potential, σ_e is the electrical conductivity, and Q_j is the volumetric heat source. For the current-conservation node, the electrical-conductivity constitutive relation was selected, and the conductivity was read directly from the material properties; for material mat1, σ_e = conductivity = 9×10^5 S·m^{-1}, which was specified as a constant.

Boundary conditions were specified as follows: a velocity inlet with an inlet gas temperature of 400 °C, a pressure outlet, and no-slip conditions at all fluid–solid interfaces. The heating-rod current was set to 7–10 A and the input power to 238–367 W. A prescribed temperature of 600–800 °C was imposed on the outer wall located at the axial center of the porous-medium reaction zone; this value represents the wall set-point temperature rather than the bed-average temperature. The model included structured meshes, second order (quadratic) Lagrange elements, and a fully coupled solver. The mesh-independence test was performed under the following conditions: porosity of 0.9, average pore diameter of 1 mm, Tr = 650 °C, input power of 303 W, CO_2:CH_4 = 1:1, GHSV = 13,000 h^{-1}, and operating pressure of 0.1 MPa. When the mesh was refined from 152,220 to 523,078 elements, the energy efficiency varied only marginally; accordingly, the mesh comprising 152,220 elements was adopted for all subsequent simulations. Heat losses through the outer surface by convection and radiation were accounted for, with an ambient temperature of 298 K and a convective heat-transfer coefficient of 10 W·m^{-2}·K^{-1}.

Reactor geometry: the total axial length was 160 mm, the outer reactor diameter was 25 mm, the central heating-rod diameter was 8 mm, and the porous reaction zone had a length of 70 mm. The overall research workflow is illustrated in Figure 1. Figure 1b shows the FC-FNN prediction model, in which the blue nodes correspond to the input layer. The yellow nodes correspond to the hidden layer. The red nodes correspond to the output layer.

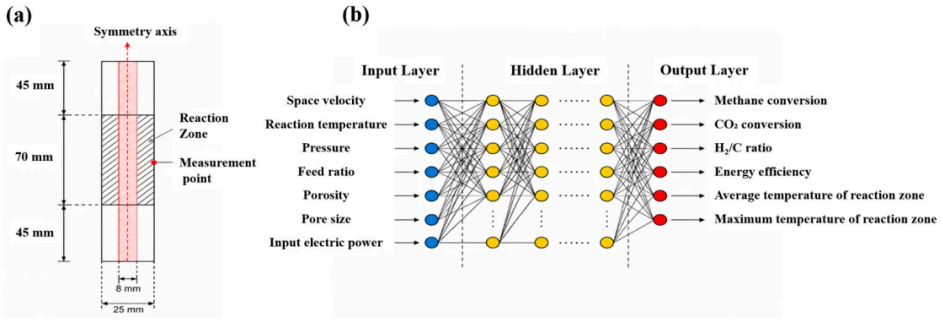


Figure 1. Geometry of resistively heated porous-medium DRM reactor and architecture of the FC-FNN surrogate model: (**a**) 2D axisymmetric geometric model; (**b**) FC-FNN prediction model.

2.2. Parameter Space and Sample Design

To investigate the coupled effects of multiple factors, seven input variables were selected, including reaction temperature, space velocity, CO_2/CH_4 feed ratio, pressure, porosity, average pore size, and input power. Their ranges are listed in Table 1. Within this parameter space, a dataset consisting of 9216 samples is generated using the numerical model for the training, testing, and subsequent optimization of the neural-network surrogate model.

Table 1. Input variables and investigated ranges.

Parameter	Symbol	Range	Description
Reaction temperature	T_r	600–800 °C	Initial set temperature at the central region of the reaction zone
Gas hourly space velocity	GHSV	6000–23,000 h^{-1}	Inlet gas hourly space velocity
CO_2/CH_4 feed ratio	R	1/3–5	Molar ratio of reactant feed
Operating pressure	p	0.1–5 MPa	Reaction operating pressure
Porosity	ε	0.70–0.95	Structural parameter of porous medium
Average pore diameter	d_p	1–4 mm	Average pore size of porous medium
Input power	P_{in}	238–367 W	Electric heating input power

3. Construction and Validation of Neural-Network Surrogate Model

3.1. Construction of the Surrogate Model

Multi-parameter optimization directly coupled to the multi-physics numerical model suffers from high computational cost. Thus, a fully connected feedforward neural network (FC-FNN) surrogate model is established to rapidly predict the reaction performance under different parameter combinations. The input layer comprises seven parameters, while the output layer includes CH_4 conversion, CO_2 conversion, energy efficiency, H_2/CO ratio, maximum temperature, and average temperature of the reaction zone, the detailed input and output variables are listed in Table 2. Temperature non-uniformity is subsequently calculated from Tmax and Tavg. The dataset is randomly shuffled and normalized for training and testing.

Table 2. Main hyperparameters of the neural network surrogate model.

Hyperparameter	Optimized Value
Network type	Fully connected feedforward neural network
Number of hidden layers	10
Number of neurons per layer	15
Activation function	Tanh
Learning rate	1.34×10^{-3}
Batch size	280
Training epochs	6000

3.2. Model Prediction Performance

To evaluate the accuracy of the surrogate model, the discrepancies between neural-network predicted values and numerical simulation values are compared. Figure 2a–f present the predicted-versus-simulated scatter plots for the main output variables. For all six outputs (CH_4 conversion, CO_2 conversion, energy efficiency, H_2/CO ratio, maximum temperature, and average temperature of the reaction zone), the data points cluster closely around the y = x line, indicating that the surrogate model can effectively capture the nonlinear mapping between the input parameters and reactor performance.

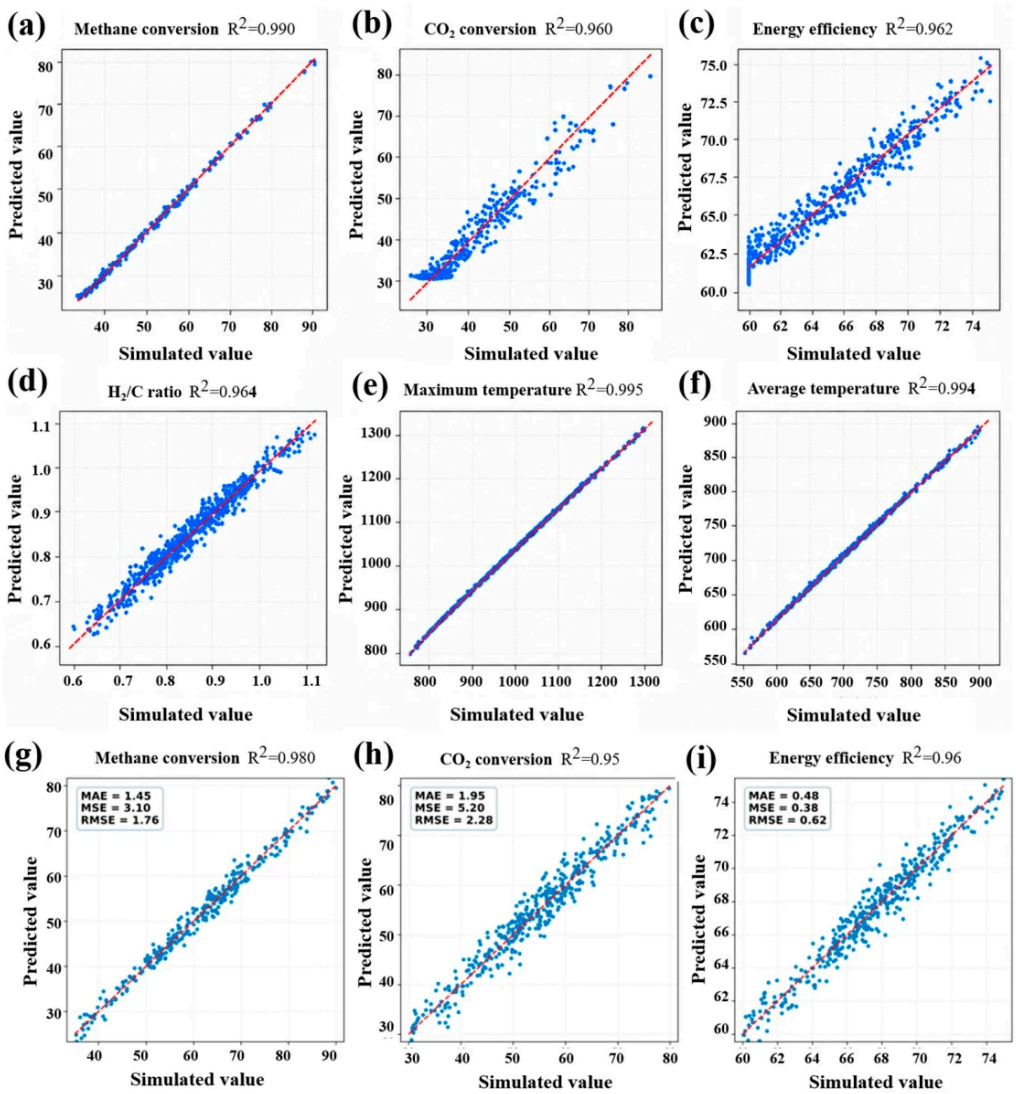


Figure 2. Parity plots of the neural network prediction results: (**a**) CH_4 conversion; (**b**) CO_2 conversion; (**c**) energy efficiency; (**d**) H_2/CO ratio; (**e**) maximum temperature in the reaction zone; (**f**) average temperature in the reaction zone; (**g**) comparison between the surrogate-model predictions and the numerical simulation values for CH_4 conversion; (**h**) comparison between the surrogate-model predictions and the numerical simulation values for CO_2 conversion; (**i**) comparison between the surrogate-model predictions and the numerical simulation values for energy efficiency.

The coefficients of determination (R^2) for CH_4 conversion, CO_2 conversion, energy efficiency, and H_2/CO ratio are generally above 0.960, demonstrating the high predictive accuracy of the model for the major performance indicators. Slight scattering is observed for the predictions of energy efficiency and H_2/CO molar ratio. This is mainly attributed to the combined influences of input power, reaction endotherm, bed temperature, and

side reactions. Similarly, Figure 2g–i present a comparison between the surrogate-model predictions and the numerical simulation values for CH_4 conversion, CO_2 conversion, and energy efficiency, with the red dashed line representing the 1:1 reference line. The predictions generally lie along the reference line, with R^2 values of 0.98, 0.95, and 0.96; MAE values of 1.45%, 1.95%, and 0.48%; and RMSE values of 1.76%, 2.28%, and 0.62%, respectively, demonstrating the good overall predictive accuracy of the surrogate model. The CO_2 conversion exhibits the most evident scattering and the lowest R^2, because CO_2 is consumed by both the primary DRM reaction and the RWGS side reaction, the latter being temperature sensitive and thus rendering the mapping more complex. In contrast, CH_4 conversion is governed mainly by the main DRM reaction and yields the best fit, whereas energy efficiency shows the smallest absolute error but slight scattering in the low-conversion region owing to variations in the heat-loss fraction.

Overall, the model accuracy is sufficient to meet the requirements of the subsequent parametric analysis and Bayesian optimization.

Figure 3 presents the experimental system, the electrified structured catalyst, and the validation results of the numerical model. Figure 3a shows the electrically heated reaction setup, while Figure 3b displays the as-fabricated electrified catalyst, whose central hole accommodates the internal heating rod. To verify the reliability of the numerical model, the simulated and experimental values of CH_4 conversion, CO_2 conversion, and the H_2/CO molar ratio were compared over the temperature range of 600–800 °C, as depicted in Figure 3c–e. As can be seen, although the simulated and experimental results exhibit certain deviations, they follow the same variational trend with temperature and are overall in good agreement.

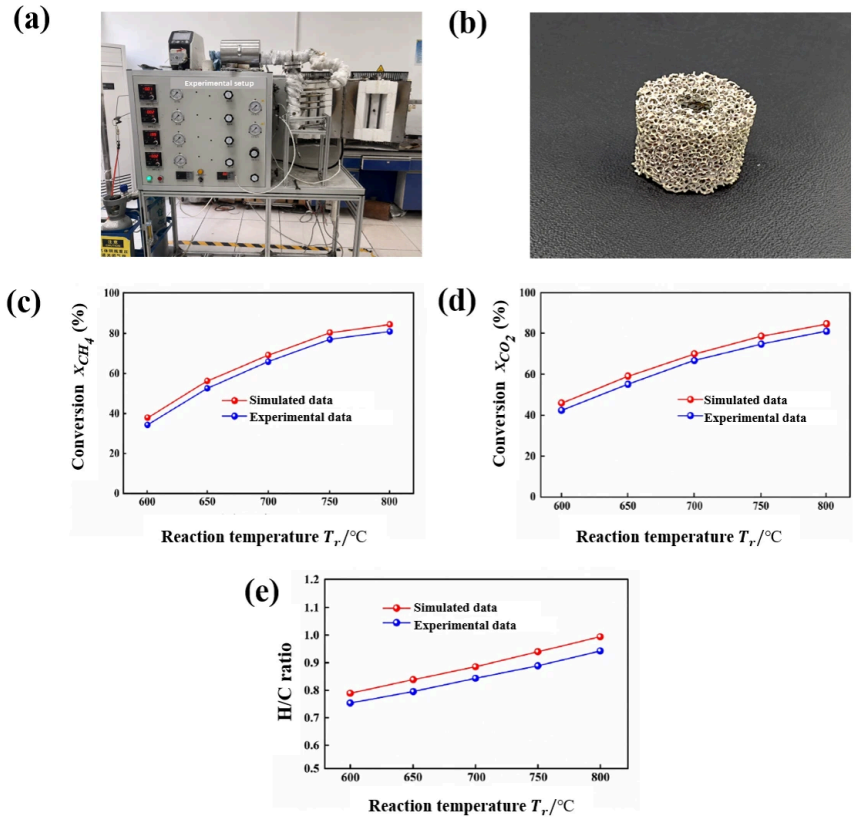


Figure 3. Experimental validation results: (**a**) photograph of the experimental setup; (**b**) photograph of the as-prepared catalyst; comparison between the simulated and experimental values of (**c**) CH_4 conversion, (**d**) CO_2 conversion, and (**e**) H_2/CO ratio.

4. Results and Discussion

4.1. Effects of Operating Parameters on DRM Performance

Figure 4 illustrates the influences of reaction temperature, gas hourly space velocity, CO_2/CH_4 feed molar ratio, and pressure on DRM performance. As shown in Figure 4a, the CH_4 and CO_2 conversions increase remarkably when the reaction temperature rises from 600 °C to 800 °C, and the H_2/CO molar ratio gradually approaches the ideal value. This is because the elevated temperature facilitates the highly endothermic main DRM reaction and accelerates the reaction rate. By contrast, the energy efficiency exhibits a non-monotonic trend, initially increasing and then decreasing with increasing temperature, indicating that excessively high temperatures increase heat loss and lower the net energy utilization.

As depicted in Figure 4b, both reactant conversions and H_2/CO molar ratio decline with the increase in gas hourly space velocity. This phenomenon mainly originates from the shortened residence time of reactants within the porous-medium reaction zone, resulting in insufficient conversion before the reactants exit the reactor. Figure 4c reveals that increasing the CO_2/CH_4 feed molar ratio improves CH_4 conversion but reduces the apparent CO_2 conversion and H_2/CO molar ratio, demonstrating that feed composition exerts simultaneous impacts on reactant utilization and syngas quality. Figure 4d indicates that higher operating pressure suppresses the conversion of CH_4 and CO_2, and decreases both H_2/CO molar ratio and energy efficiency, suggesting that elevated pressure is unfavorable for achieving sufficient DRM conversion under the investigated conditions.

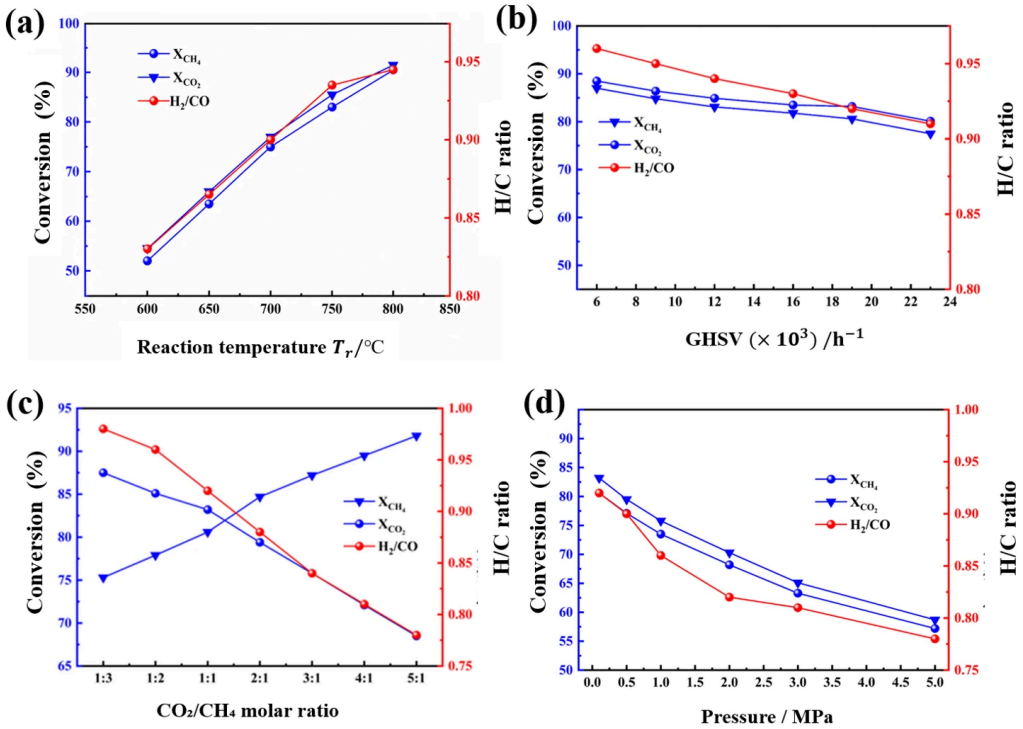


Figure 4. Effects of operating conditions on DRM performance: (**a**) reaction temperature; (**b**) GHSV; (**c**) CO_2/CH_4 feed ratio; (**d**) pressure.

Figure 5 illustrates the influences of different operating parameters on the temperature distribution within the reaction zone and energy efficiency. As shown in Figure 5a, both the maximum and average temperatures of the reaction zone increase markedly with increasing reaction temperature, indicating that elevating the reaction temperature improves the overall thermal level of the porous-medium reaction zone. Additionally, the energy efficiency

initially increases and then slightly decreases, suggesting that excessively high temperatures increase heat loss and thereby diminish the benefit of further temperature elevation.

Figure 5b demonstrates that the maximum reaction temperature, average reaction temperature, and energy efficiency gradually decrease as the GHSV increases. This is attributed to the shortened residence time of reactants in the catalyst bed, together with an enhanced heat-carrying effect of the flowing gas, which suppresses heat accumulation inside the reaction zone. As presented in Figure 5c, the overall reaction-zone temperature decreases with the increase in CO_2/CH_4 feed molar ratio, whereas the energy efficiency first rises and then declines, peaking near a ratio of 1:1. This suggests that an appropriate feed ratio facilitates the matching between reaction endothermic demand and electric heating supply. Figure 5d shows that increasing operating pressure reduces both reaction-zone temperature and energy efficiency, implying that high pressure is unfavorable for DRM and degrades the energy efficiency of the Joule-heated system.

Overall, higher reaction temperature, lower gas hourly space velocity, feed molar ratio close to 1:1, and low-pressure conditions are beneficial to improving the comprehensive performance of the resistively heated porous-medium DRM reactor.

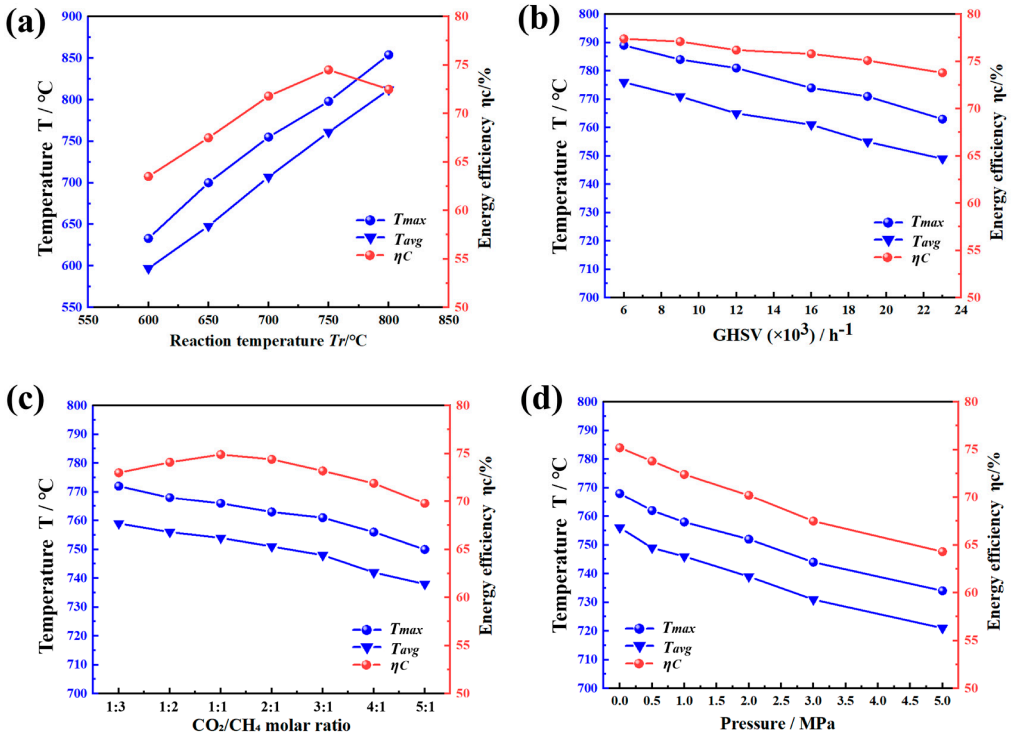


Figure 5. Effects of operating parameters on the reaction-zone temperature and energy efficiency: (**a**) reaction temperature; (**b**) GHSV; (**c**) feed ratio; (**d**) pressure.

4.2. Effects of Porous-Medium Structural Parameters on DRM Performance

Porous-medium structural parameters regulate the DRM performance by modulating the effective thermal conductivity, gas–solid contact area, flow resistance, and local heat transfer in the bed. Figure 6 presents the effects of porosity and average pore diameter on the reaction-zone temperature distribution, reactant conversion, H_2/CO molar ratio, and energy efficiency.

As illustrated in Figure 6a,b, at a given porosity, both the maximum and average temperatures of the reaction zone gradually decrease as the average pore diameter increases, because larger pore sizes weaken gas–solid heat exchange and the thermal-storage capacity of the bed. Furthermore, increasing porosity elevates the local maximum temperature yet

reduces the average reaction-zone temperature. This implies that high porosity weakens the thermal conduction of the solid skeleton and the overall heat-storage capacity, which tends to cause local heat accumulation.

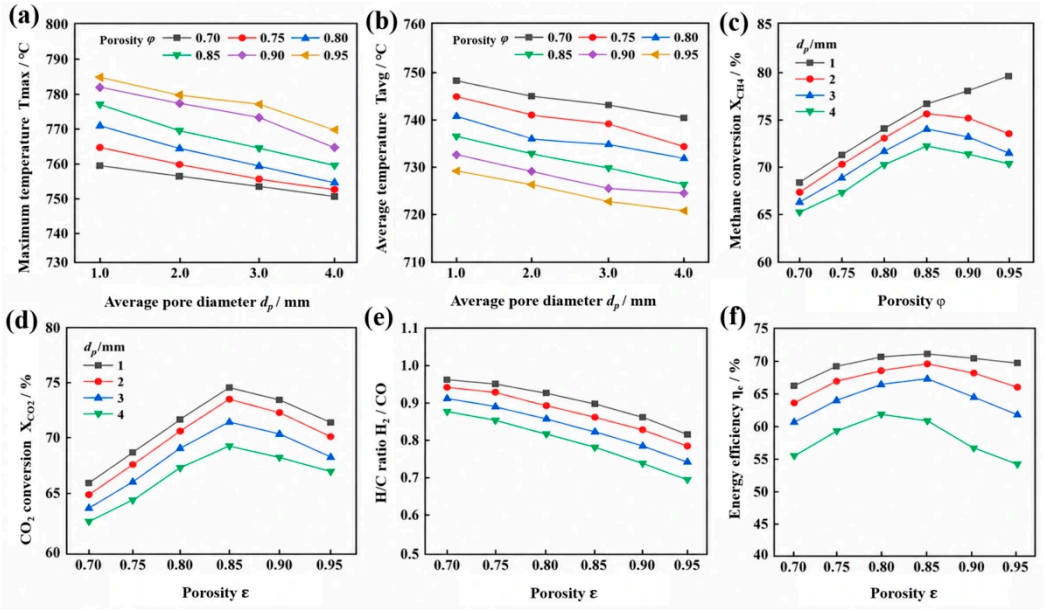


Figure 6. Effects of porosity and average pore size on DRM performance: (**a**) maximum temperature of the reaction zone; (**b**) average temperature of the reaction zone; (**c**) CH_4 conversion; (**d**) CO_2 conversion; (**e**) H_2/CO ratio; (**f**) energy efficiency.

As shown in Figure 6c,d, both CH_4 and CO_2 conversion exhibit an overall non-monotonic dependence on porosity, first rising and then declining, with relatively high conversion achieved at $\varepsilon \approx 0.85$. Smaller average pore sizes correspond to higher reactant conversion, indicating that smaller pores provide a larger gas–solid contact area and thereby facilitate reactant conversion.

Figure 6e shows that the H_2/CO ratio decreases with increasing porosity and average pore size, indicating that excessively high porosity and larger pore sizes weaken the main DRM reaction and shift the product composition away from the ideal syngas ratio. Figure 6f shows that energy efficiency also exhibits a pronounced non-monotonic dependence on the porous-media parameters, with higher values obtained at moderate porosity and smaller pore sizes. Overall, moderate porosity combined with a small average pore diameter can balance reactant conversion, product composition, and energy utilization efficiency. The preferable structural range for the porous medium is approximately $\varepsilon \approx 0.85$ and d_p = 1–2 mm.

4.3. Effect of Input Power on DRM Performance

Figure 7 illustrates the effects of input power on the reaction performance and thermal characteristics of the Joule-heated porous-medium DRM reactor. As shown in Figure 7a, both CH_4 and CO_2 conversions increase slowly as the input power rises from 238 W to 367 W, accompanied by a slight improvement in the H_2/CO molar ratio. This indicates that higher input power strengthens the heat supply of the reaction zone and promotes the main DRM reaction. However, the conversion gain is modest in this range, suggesting that the reaction is already approaching a high conversion level and further power input yields little additional benefit. As shown in Figure 7b, both the maximum and average temperatures of the reaction zone gradually increase with increasing input power, reflecting a higher overall bed temperature.

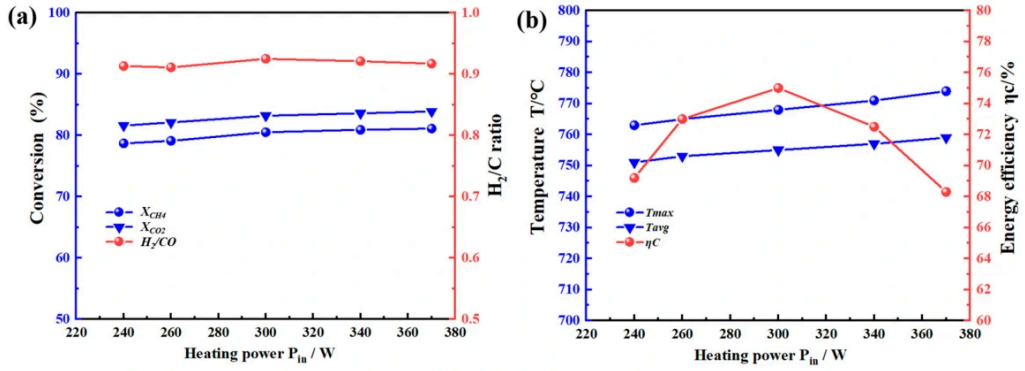


Figure 7. Effects of input power on reaction performance and thermal characteristics: (**a**) CH_4/CO_2 conversion and H_2/CO ratio; (**b**) reaction-zone temperature and energy efficiency.

In contrast to the monotonically rising temperature, energy efficiency initially increases and then decreases with increasing input power, peaking near 303 W. At low power, the heat supply is insufficient to drive the reaction; at excessive power, however, the extra input is lost as heat rather than converted usefully into reaction enthalpy. Therefore, a higher input power does not necessarily lead to better overall performance, and an appropriate balance between reactant conversion and energy efficiency is required.

4.4. Parameter Sensitivity Analysis

Figure 8 presents the global sensitivity analysis of input parameters for energy efficiency, average conversion, H_2/CO molar ratio, and temperature non-uniformity. The dominant factors differ markedly across the four indicators. For energy efficiency, GHSV, CO_2/CH_4 feed molar ratio, and operating pressure exhibit high sensitivity, implying that energy utilization is mainly governed by residence time, reactant ratio, and thermodynamic equilibrium. For average conversion, reaction temperature, CO_2/CH_4 feed molar ratio, and operating pressure make major contributions, which means reactant conversion is jointly controlled by thermal driving force and reaction equilibrium. The H_2/CO molar ratio is predominantly affected by GHSV and CO_2/CH_4 feed molar ratio, because the product composition is tied to residence time and feed composition.

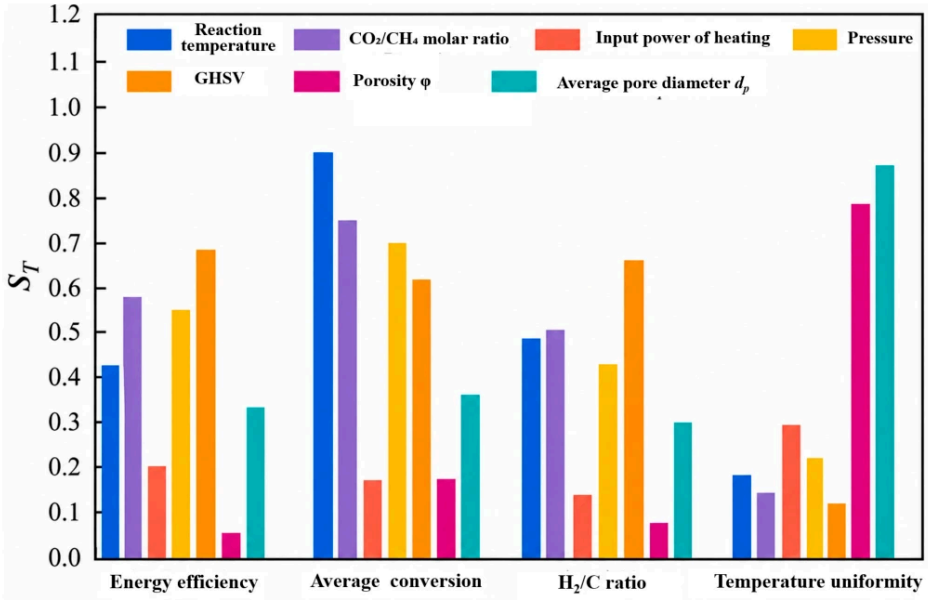


Figure 8. Global sensitivity analysis of input parameters with respect to energy efficiency, average reactant conversion, H_2/CO ratio, and temperature non-uniformity.

In contrast, temperature non-uniformity is mainly governed by porosity and average pore diameter, demonstrating that porous-medium structural parameters are critical for regulating bed temperature distribution. Overall, operating parameters mainly determine reaction conversion and energy efficiency, while structural parameters dominate temperature non-uniformity. Accordingly, the synergistic effect of operating conditions and porous-structure parameters should be considered in subsequent optimization.

4.5. Bayesian Optimization Results

Based on the neural network surrogate model, Bayesian optimization was employed for parameter optimization. First, with energy efficiency as the optimization objective, the iterative performance of Gaussian process regression-based Bayesian optimization (GPR-BO) was compared with that of random search. As shown in Figure 9a, GPR-BO rapidly identifies the high-energy-efficiency region during the early optimization stage and achieves better results than random search with fewer iterations. The solid lines denote the mean best-so-far objective value obtained from ten independent runs initialized with different random seeds. For both subfigures, the orange lines correspond to the proposed Bayesian optimization approach (GPR-BO in (a), UCA-BO in (b)) and the green lines denote random search under the same computational budget.

Further considering the requirements for syngas quality and temperature distribution, UCA-BO is employed to optimize the average reactant conversion under the constraints of $H_2/CO \geq 0.9$ and temperature non-uniformity $\leq 5\%$. As shown in Figure 9b, compared with random search, UCA-BO more efficiently explores the high-conversion region that satisfies the imposed constraints and achieves a higher average reactant conversion within a limited number of iterations.

The UCA-BO optimum comprises a reaction temperature of 784 °C; GHSV = 10,024 h^{-1}; operating pressure of 0.23 MPa; CO_2/CH_4 feed molar ratio of 0.45; porosity of 0.89; average pore diameter of 1.2 mm; and input power of 324 W. Under this set of parameters, UCA-BO predicts an average conversion of 94.12%, a H_2/CO molar ratio of 0.98, temperature non-uniformity of 4.53%, and energy efficiency of 74.83%. To verify these predictions, the same parameter set is re-evaluated with the high-fidelity numerical model (posterior verification); the results are listed in Table 3.

Table 3. Comparison between optimized results and posterior verification.

Index	Best Value of Numerical Simulation Samples	UCA-BO Optimized Value	Improvement Magnitude R/%	Posterior Verification Value
H_2/CO	0.95	0.98	3.16	0.91
Temperature non-uniformity	5.00%	4.53%	−9.40	4.86%
Average conversion under constraints	85.67%	94.12%	9.86	91.28%
Energy efficiency	71.62%	74.83%	4.48	72.36%

As can be seen from Table 3, the UCA-BO optimized values show improvements in all performance indicators compared with the optimal values from numerical simulation samples. Specifically, the constrained average conversion increases from 85.67% to 94.12%, and the energy efficiency rises from 71.62% to 74.83%, while temperature non-uniformity decreases from 5.00% to 4.53%. The posterior validation results give a H_2/CO ratio of 0.91, a temperature non-uniformity of 4.86%, an average reactant conversion of 91.28%, and an energy efficiency of 72.36%. Although the posterior validation results exhibit some deviations from the UCA-BO predictions, all performance indicators remain within the

imposed constraints of $H_2/CO \geq 0.9$ and temperature non-uniformity $\leq 5\%$, demonstrating the reliability of the optimization results to a certain extent.

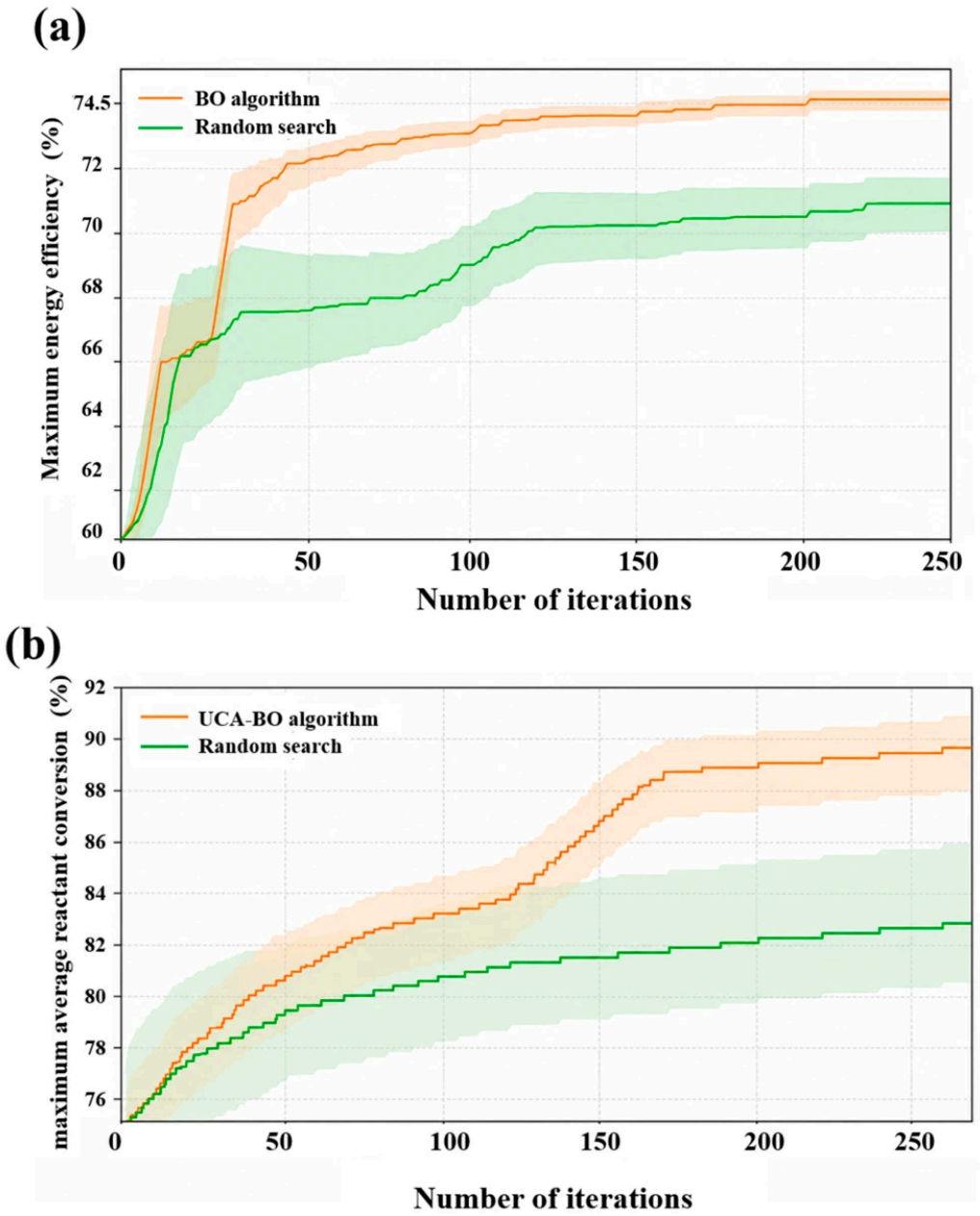


Figure 9. Optimization histories of Bayesian optimization and random search: (**a**) energy efficiency optimization; (**b**) average conversion optimization constrained by H_2/CO and temperature non-uniformity. The shaded regions represent ± 1 standard deviation across these ten runs.

As can be seen from Tables 4 and 5, all five independent recalculation points satisfy the constraints of $H_2/CO \geq 0.90$ and temperature non-uniformity $\leq 5\%$. Among them, Case V3 lies closest to the constraint boundary, with $H_2/CO = 0.90$ and temperature non-uniformity of 4.94%. Its maximum relative error remains below 10%, demonstrating that a feasible region exists around the optimum.

Table 4. Five independent local validation cases near the optimum.

Case	T/°C	GHSV/h^{-1}	P/MPa	CO_2/CH_4	ε	d_p/mm	P_{in}/W
V1	784.0	10,024	0.2300	0.4500	0.8900	1.200	324.0
V2	744.8	10,525	0.2415	0.4275	0.8455	1.260	307.8
V3	800.0	9523	0.2185	0.4725	0.9345	1.140	340.2
V4	768.3	10,275	0.2243	0.4612	0.8678	1.230	315.9
V5	795.8	9773	0.2357	0.4387	0.9122	1.170	332.1

Table 5. Output results of five independent local validation cases.

Case	H_2/CO	Temperature Non-Uniformity/%	Average Conversion/%	Energy Efficiency/%	Maximum Relative Error/%	Constraint
V1	0.91	4.86	91.28	72.36	7.28	Satisfied
V2	0.93	4.72	90.65	71.88	6.42	Satisfied
V3	0.90	4.94	89.76	71.25	8.63	Satisfied
V4	0.92	4.68	92.10	72.02	6.91	Satisfied
V5	0.94	4.79	90.82	71.63	7.56	Satisfied

As illustrated by the box plot in Figure 10, the deviation distribution gradually widens with increasing perturbation intensity. Under 10% perturbation, a small number of tail values of approximately ±10–15% are observed, while most samples remain concentrated within a low deviation range. Combined with the independent local recalculation results, these findings demonstrate that although the optimum lies close to the constraint boundary, it maintains certain robustness under minor parameter fluctuations. Appropriate safety margins for the H_2/CO ratio and temperature uniformity should be reserved in practical operation.

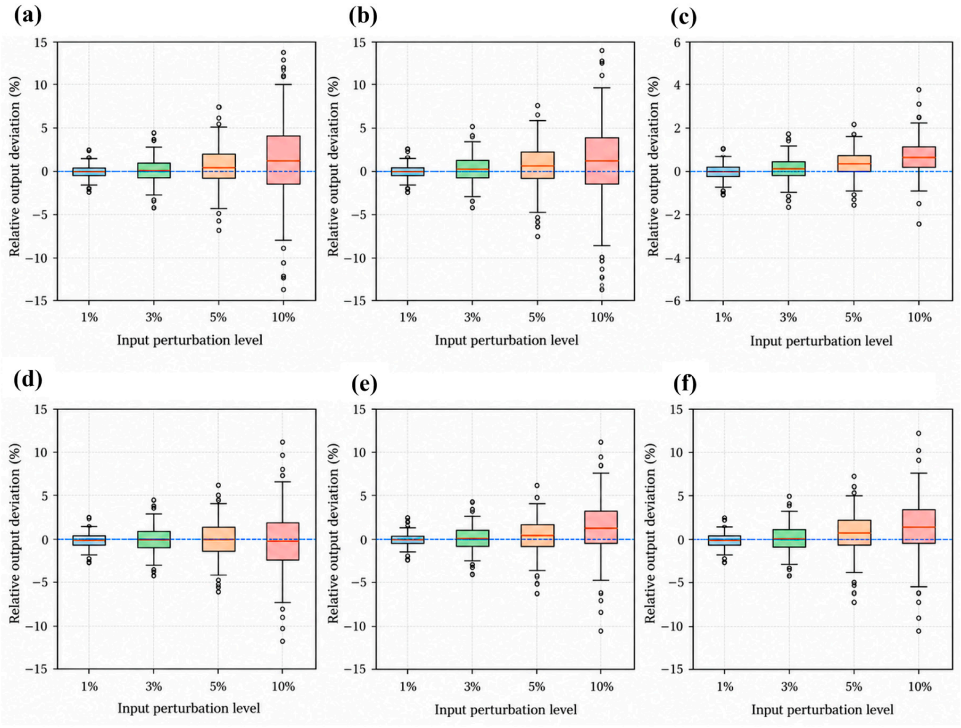


Figure 10. Statistical distribution of relative output deviations under different perturbation levels. (**a**) Methane conversion, (**b**) CO2conversion, (**c**) Energy efficiency, (**d**) H2/CO ratio, (**e**) Maximum temperature, (**f**) Average temperature.

4.6. Comparison of Constrained Single-Objective Bayesian Optimization

To further elucidate the synergy among high reactant conversion, high energy efficiency, and temperature non-uniformity in the resistively heated system, Figure 11 compares the best values from the original numerical simulation samples, the UCA-BO predictions, and the posterior validation results. Improvement magnitude R: H_2/CO molar ratio +3.16%, 9.40% reduction in temperature non-uniformity, constrained average conversion +9.86%, and energy efficiency +4.48%.

The UCA-BO predictions outperform the optimal original samples in terms of average conversion and energy efficiency, with temperature non-uniformity maintained below 5%. This demonstrates that the optimization does not simply pursue higher reactant conversion but achieves an overall performance improvement under constraints on syngas quality and thermal-field distribution.

According to the posterior verification results, the energy efficiency increases from 71.62% (original sample optimum) to 72.36%, and temperature non-uniformity reaches 4.86%, which is still below the constraint threshold. Additionally, the H_2/CO molar ratio is 0.91, complying with the syngas quality constraint. The posterior verification outputs are lower than the UCA-BO predictions, suggesting that the surrogate model introduces approximation errors within the continuous optimization space.

Accordingly, the optimized parameters can serve as preliminary guidance for reactor structural design and operating-condition screening. Further validation should be carried out with locally augmented sampling and experimental tests on physical reactors in follow-up work.

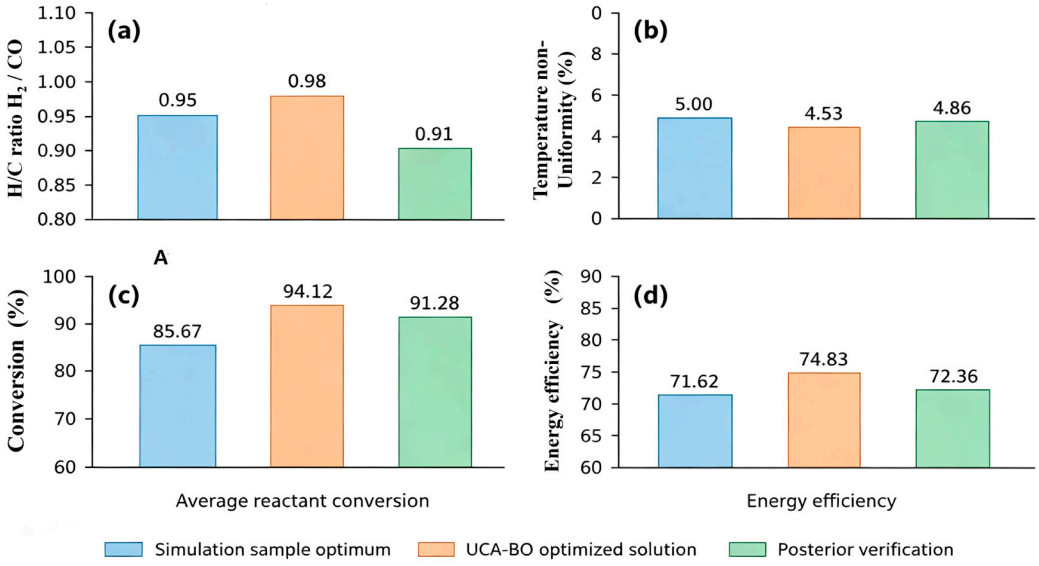


Figure 11. Comparison of energy efficiency, temperature non-uniformity, and constraint-related metrics before and after optimization. (**a**) H_2/CO ratio, (**b**) Temperature non-uniformity, (**c**) Average reactant conversion, (**d**) Energy efficiency.

5. Conclusions

In this work, a numerical model for Joule-heated porous-medium methane dry reforming is established, and a fully connected feedforward neural-network surrogate model trained on 9216 samples accurately predicts the main reaction performance indicators, with R^2 generally above 0.960 and MAE/RMSE within acceptable ranges. The initial set temperature, GHSV, CO_2/CH_4 feed ratio, and operating pressure govern the residence time, reaction rate, chemical equilibrium, and heat utilization, and thus determine the conversion and energy efficiency. In contrast, porosity and average pore diameter affect tempera-

ture non-uniformity and syngas quality by altering the effective bed thermal conductivity, gas–solid contact area, and flow behavior. Sobol analysis further shows that different performance indicators are controlled by different dominant parameters, so that operating and structural variables must be optimized jointly. Under the constraints of $H_2/CO > 0.9$ and temperature non-uniformity <5%, UCA-BO predicts an optimum with average conversion 94.12%, H_2/CO ratio 0.98, temperature non-uniformity 4.53%, and energy efficiency 74.83%. Posterior verification with the high-fidelity numerical model yields slightly lower values of 91.28%, 0.91, 4.86%, and 72.36%, respectively, a deviation attributable to the inherent approximation error of the surrogate over the continuous optimization domain. Nevertheless, all verified metrics satisfy the imposed constraints, confirming the reliability of the optimized design.

Author Contributions: Y.R.: conceptualization and writing—original draft preparation; D.T.: methodology; L.Z.: software, validation, and conceptualization; H.M.: formal analysis and investigation; M.C.: data curation; Z.L.: supervision and writing—reviewing and editing; X.D.: supervision and writing—review and editing. All authors have read and agreed to the published version of the manuscript.

Funding: This research was funded by the Nantong Social Science Fund, grant number SKB26-26.

Data Availability Statement: The original contributions presented in this study are included in the article. Further inquiries can be directed to the corresponding author.

Conflicts of Interest: The authors declare no conflicts of interest.

References

1. Verykios, X.E. Catalytic dry reforming of natural gas for the production of chemicals and hydrogen. *Int. J. Hydrogen Energy* **2003**, *28*, 1045–1063. [CrossRef]
2. Hussien, A.G.S.; Polychronopoulou, K. A review on the different aspects and challenges of the dry reforming of methane (DRM) reaction. *Nanomaterials* **2022**, *12*, 3400. [CrossRef] [PubMed]
3. Subramanian, S.; Song, Y.; Kim, D.; Yavuz, C.T. Redox and nonredox CO_2 utilization: Dry reforming of methane and catalytic cyclic carbonate formation. *ACS Energy Lett.* **2020**, *5*, 1689–1700. [CrossRef]
4. Pakhare, D.; Spivey, J. A review of dry reforming of methane over noble metal catalysts. *Chem. Soc. Rev.* **2014**, *43*, 7813–7837. [CrossRef] [PubMed]
5. Abdullah, B.; Abd Ghani, N.A.; Vo, D.V.N. Recent advances in dry reforming of methane over Ni-based catalysts. *J. Clean. Prod.* **2017**, *162*, 170–185. [CrossRef]
6. Chen, H.; Shao, Y.; Mu, Y.; Xiang, H.; Zhang, R.; Chang, Y.; Hardacre, C.; Wattanakit, C.; Jiao, Y.; Fan, X. Structured silicalite-1 encapsulated Ni catalyst supported on SiC foam for dry reforming of methane. *AIChE J.* **2021**, *67*, e17126. [CrossRef]
7. Wismann, S.T.; Engbæk, J.S.; Vendelbo, S.B.; Bendixen, F.B.; Eriksen, W.L.; Aasberg-Petersen, K.; Frandsen, C.; Chorkendorff, I.; Mortensen, P.M. Electrified methane reforming: A compact approach to greener industrial hydrogen production. *Science* **2019**, *364*, 756–759. [CrossRef] [PubMed]
8. Kim, Y.T.; Lee, J.J.; Lee, J. Electricity-driven reactors that promote thermochemical catalytic reactions via Joule and induction heating: A review. *Chem. Eng. J.* **2023**, *470*, 144333. [CrossRef]
9. Zheng, L.; Ambrosetti, M.; Tronconi, E. Joule-heated catalytic reactors toward decarbonization and process intensification: A review. *ACS Eng. Au* **2024**, *4*, 4–21. [CrossRef]
10. Zhu, Z.; Zhang, S.; Xiao, L. Numerical study of methane dry reforming in an electromagnetic induction heating reactor. *Appl. Therm. Eng.* **2025**, *280*, 128514. [CrossRef]
11. Lin, Y.X.; Yang, C.; Zhang, W.; Machida, H.; Norinaga, K. Lattice Boltzmann study on the effect of hierarchical pore structure on fluid flow and coke formation characteristics in open-cell foam for dry reforming of methane. *Chem. Eng. Sci.* **2023**, *268*, 118380. [CrossRef]
12. Weng, J.Q.; Akbar, A.; Deng, Q.H.; Ye, G.H.; Zhou, X.G.; Yuan, W.K. Enhanced performance of packed bed methane dry reformers using metal foam catalyst pellets: A particle resolved CFD study. *Chem. Eng. Sci.* **2024**, *291*, 119897. [CrossRef]
13. Nield, D.A.; Bejan, A. *Convection in Porous Media*, 5th ed.; Springer: New York, NY, USA, 2017.
14. Alotaibi, F.N.; Berrouk, A.S.; Muhammad, S. Optimization of yield and conversion rates in methane dry reforming using artificial neural networks and the multiobjective genetic algorithm. *Ind. Eng. Chem. Res.* **2023**, *62*, 17268–17285. [CrossRef]

15. Li, J.Y.; Xu, J.; Rebrov, E.; Bogaerts, A. Machine learning-based prediction and optimization of plasma-catalytic dry reforming of methane in a dielectric barrier discharge reactor. *Chem. Eng. J.* **2025**, *507*, 159897. [CrossRef]
16. Cherif, A.; Atwair, M.; Atsbha, T.A.; Zarei, M.; Duncan, I.J.; Nebbali, R.; Sen, F.; Lee, C.J. Enabling low-carbon membrane steam methane reforming: Comparative analysis and multi-objective NSGA-II-integrated Bayesian optimization. *Energy Convers. Manag.* **2023**, *297*, 117718. [CrossRef]
17. Alsaffar, M.A.; Ayodele, B.V.; Mustapa, S.I. Scavenging carbon deposition on alumina supported cobalt catalyst during renewable hydrogen-rich syngas production by methane dry reforming using artificial intelligence modeling technique. *J. Clean. Prod.* **2019**, *240*, 119168. [CrossRef]
18. Modest, M.F. Radiative Heat Transfer. *Int. J. Heat Mass Transf.* **2013**, 62–64. [CrossRef]
19. Menter, F.R. Two-equation eddy-viscosity turbulence models for engineering applications. *AIAA J.* **1994**, *32*, 1598–1605. [CrossRef] [PubMed]

Disclaimer/Publisher's Note: The statements, opinions and data contained in all publications are solely those of the individual author(s) and contributor(s) and not of MDPI and/or the editor(s). MDPI and/or the editor(s) disclaim responsibility for any injury to people or property resulting from any ideas, methods, instructions or products referred to in the content.